Induced Electrokinetic Transport in Micro−Nanofluidic Interconnect Devices

Xiaozhong Jin,† Sony Joseph,† Enid N. Gatimu,‡ Paul W. Bohn,‡ and N. R. Aluru*,†

Beckman Institute for Advanced Science and Technology, University of Illinois at Urbana−Champaign, Urbana, Illinois 61801

Received July 31, 2007. In Final Form: September 25, 2007

Hybrid micro−nanofluidic interconnect devices can be used to control analyte transfer from one microchannel to the other through a nanochannel under rest, injection, and recovery stages of operation by varying the applied potential bias. Using numerical simulations based on coupled transient Poisson−Nernst−Planck and Stokes equations, we examine the electrokinetic transport in a gateable device consisting of two 100 μm long, 1 μm wide negatively charged microchannels connected by a 1 μm long, 10 nm wide positively charged nanochannel under both positive and negative bias potentials. During injection, accumulation of ions is observed at the micro−nano interface region with the positive potential and depletion of ions is observed at the other micro−nano junction region. Net space charge in the depletion region gives rise to nonlinear electrokinetic transport during the recovery stage due to induced pressure, induced electroosmotic flow of the second kind, and complex flow circulations. Ionic currents are computed as a function of time for both positive and negative bias potentials for the three stages. Analytical expressions derived for ion current variation are in agreement with the simulated results. In the presence of multiple accumulation or depletion regions, we show that a hybrid micro−nano device can be designed to function as a logic gate.

1. Introduction

During the past 1−2 decades, microfluidic devices have been developed extensively for chemical and biological sensing, sample separation, mixing, and drug delivery.[1,2] More recently, nanofluidic channels and systems, where the thickness of the electrical double layer can be comparable to the characteristic channel width, have been fabricated to explore new avenues for the manipulation of chemical species.[3−9] Integrated microchannel−nanochannel systems, functionalized as gateable interconnects to control transport of species, are the building blocks of hybrid architectures for multilayered separation systems.[10−14] In the hybrid microfluidic−nanofluidic systems, the surface charge of the nanochannel plays a significant role in controlling ionic transport, especially when the Debye length is comparable to the nanochannel width.[15−17] As the pore size of the membrane approaches nanometer scale, the nanochannel surface charge determines the direction of the fluid flow, and significant sample stacking phenomena have been observed with 15 nm pore diameter polycarbonate membranes.[11] By a simple manipulation of the physical design of the micro−nano channels, rapid and complete mixing has been achieved in the micro−nano junction region.[13] Nanofluidic filters connecting microchannels have been used to demonstrate a highly efficient microfluidic sample preconcentration device[7] based on an electrokinetic trapping mechanism. In a nanometer-sized channel, the extension of the electrical double layer results in the depletion of co-ions and enrichment of counterions, which can be explained by the classical Donnan exclusion principle.[18] With an applied electrical field, ion enrichment and depletion phenomena have been observed in the micro−nano junction region.[9] The ion enrichment and depletion induced in the junction next to the ion-permselective membrane is not completely understood at present, although a common qualitative description of the phenomenon summarized from the literature is given in ref 19. This phenomenon, also known as concentration polarization, has been previously observed in ion-exchange membranes[20] and is known to induce nonlinear electrokinetic transport. Experiments have shown that induced pressure can play a significant role in the electrokinetic transport in devices with interconnect regions.[21] Although experiments have indicated that induced electrokinetic phenomena are present in the micro−nano junction regions, a comprehensive picture of the role of the micro−nano junction region and the underlying physical phenomena behind the atypical transient ionic current variation, induced pressure driven flow, and the induced electroosmotic flow due to space charges in the junction region is still lacking. An understanding of such induced

* To whom correspondence should be addressed. E-mail: aluru@uiuc.edu. Web: http://www.uiuc.edu/aluru.

† University of Illinois at Urbana−Champaign.

‡ Department of Chemical and Biomolecular Engineering, University of Notre Dame.

(1) Hong, J. W.; Quake, S. R. *Nat. Biotechnol.* **2003**, *21*, 1179−1183.
(2) Yao, S.; Myers, A. M.; Posner, J. D.; Rose, K. A.; Santiago, J. G. *J. Microelectromech. Syst.* **2006**, *15*, 717−728.
(3) Yaroshchuk, A.; Zhukowa, O.; Ulbricht, M.; Ribitsch, V. *Langmuir* **2005**, *21*, 6872−6882.
(4) Eijkel, J. C. T.; van den Berg, A. *Microfluid Nanofluid* **2005**, *1*, 249−267.
(5) Jong, J. de.; Lammertink, R. G. H.; Wessling, M. *Lab Chip* **2006**, *6*, 1125−1139.
(6) Jeon, S.; Malyarchuk, V.; White, J. O.; Rogers, J. A. *Nano Lett.* **2005**, *5*, 1351−1356.
(7) Wang, Y.; Stevens, A. L.; Han, J. *Anal. Chem.* **2005**, *77*, 4293−4299.
(8) Fan, R.; Yue, M.; Karnik, R.; Majumdar, A.; Yang, P. *Phys. Rev. Lett.* **2005**, *95*, 086607.
(9) Pu, Q.; Yun, J.; Temkin, H.; Liu, S. *Nano Lett.* **2004**, *4*, 1099−1103.
(10) Kuo, T. C.; Cannon, D. M.; Chen, Y.; Tulock, J. J.; Shannon, M. A.; Sweedler, J. V.; Bohn, P. W. *Anal. Chem.* **2003**, *75*, 1861−1867.
(11) Kuo, T. C.; Cannon, D. M.; Shannon, M. A.; Bohn, P. W.; Sweedler, J. V. *Sens. Actuators* **2003**, *102*, 223−233.
(12) Tulock, J. J.; Shannon, M. A.; Bohn, P. W.; Sweedler, J. V. *Anal. Chem.* **2004**, *76*, 6419−6425.
(13) Kuo, T. C.; Kim, H. K.; Cannon, D. M.; Shannon, M. A.; Sweedler, J. V.; Bohn, P. W. *Angew. Chem., Int. Ed.* **2004**, *43*, 1862−1865.
(14) Gatimu, E. N.; Sweedler, J. V.; Bohn, P. W. *Analyst* **2006**, *131*, 705−709.
(15) Schoch, R. B.; Lintel, H. V.; Renaud, P. *Phys. Fluids* **2005**, *17*, 100604.
(16) Schoch, R. B.; Renaud, P. *Appl. Phys. Lett.* **2005**, *86*, 253111.
(17) Stein, D.; Kruithof, M.; Dekker, C. *Phys. Rev. Lett.* **2004**, *93*, 035901.
(18) Plecis, A.; Schoch, R. B.; Renaud, P. *Nano Lett.* **2005**, *5*, 1147−1155.
(19) Baldessari, F.; Santiago, J. G. *J. Nanobiotechnol.* **2006**, *4*, 12.
(20) Probstein, R. F. *Physicochemical Hydrodynamics*, 2nd ed.; John Wiley and Sons, Inc.: New York, 1994.
(21) Sniadecki, N. J.; Lee, C. S.; Sivanesan, P.; DeVoe, D. L. *Anal. Chem.* **2004**, *76*, 1942−1947.

10.1021/la702326v CCC: $37.00
Published on Web 11/14/2007

electrokinetic phenomena in hybrid micro−nano channels is essential for designing and fabricating integrated nanofluidic−microfluidic systems.

Even though great strides have been made toward fabricating integrated nanofluidic−microfluidic channels, precision fabrication and highly reliable measurements at length scales of a few nanometers are still a challenge. Modeling and simulation can predict experimental data beforehand and could be of immense help in explaining underlying physical mechanisms observed in experiments. Molecular dynamics (MD) simulations have been shown to be useful in studying the ionic transport and electroosmotic flow in small diameter nanochannels (3.5 nm down to 0.95 nm).[22−27] However, computational cost excludes the possibility of the MD simulation for devices with dimensions greater than 10 nm. MD simulations have shown that ion mobilities are different from the bulk value typically in a region within 1 nm from the wall surface.[25,27] At channel widths greater than 10 nm, continuum theory, which statistically averages the atomic interactions, has often been used to calculate the electrokinetic transport. Most continuum models describe the ionic transport by the Poisson and the Nernst−Planck equations (PNP). A review of theory and simulations of fundamental studies in nanochannels is given in refs 19 and 28. A simplified version of the PNP equations is often used as a 1D network model for solving transient ionic transport through an ion-exchange membrane.[29,30] Although the phenomenon of concentration polarization has been demonstrated in ion-exchange membranes by transient 1D models, in micro−nano hybrid devices, a 1D model that does not consider a variation of electrostatic potential and concentration gradients across the channel width is not capable of resolving the double layer in the nanochannel. Steady-state PNP equations were solved in a 2D domain (30 nm, 6 μm nanochannel with two 1 μm × 1 μm baths) to capture the double-layer effect in the nanochannel and obtain steady-state $I-V$ curves.[31] For the same geometry, steady-state PNP coupled with the Navier−Stokes equations were solved for an energy conversion device operated under an external pressure gradient.[32] However, transient PNP and Navier−Stokes (or Stokes) equations have not been applied to modeling a system consisting of sufficiently long microchannels, which is essential to understand the ion enrichment and depletion effects in a micro−nano interconnect device.

In this paper, we present for the first time, transient numerical simulations in a micro−nano interconnect device to capture the transient phenomena, unique ion current signatures, and induced convective transport in the microchannel that arise due to the ion enrichment−depletion phenomena at the interfaces between the nanochannel and the microchannel. A transient coupled PNP−Stokes system is solved in a nanofluidic channel (1 μm length, 10 nm width) connecting two microchannels (100 μm length, 1 μm width) with electric potentials applied at the ends of the microfluidic channels to drive the fluid. The simulations are based on the experimental setup in ref 14 consisting of two microchannels connected by a nanochannel with three stages of device operation, i.e., rest, injection, and recovery stages. A fundamental understanding of the electrokinetic transport in the micro−nano interconnect is critical for the design of micro−nanofluidic devices which can function as gating, sensing, preconcentration, and separation devices.

The rest of this paper is outlined as follows. Section 2 presents the theory and the mathematical model, Section 3 describes the hybrid micro−nano device and the simulation details, and Section 4 presents extensive results on the three stages of the operation of the hybrid micro−nano device. Finally, conclusions are given in Section 5.

2. Theory

In this section, a description of the complete set of equations that are used for simulation of electrokinetic transport in hybrid micro−nanofluidic channels is presented. More extensive details and the assumptions underlying these theories can be found in ref 33. When the flow is electrically driven, the total flux consists of three terms: a diffusive component resulting from the concentration gradient, an electrophoretic component, which stems from the electrical potential gradient, and a convective component which originates from the fluid flow. The total flux of the ith species is given by the expression

$$\Gamma_i = -D_i\nabla c_i - \Omega_i z_i F c_i \nabla\phi + c_i\mathbf{u} \tag{1}$$

where F is the Faraday's constant, z_i is the valence, D_i is the diffusion coefficient, Ω_i is the ionic mobility, Γ_i is the flux, c_i is the concentration of the ith species, $\mathbf{u}$ is the velocity vector of the bulk flow, and ϕ is the electrical potential. The three terms on the right-hand side of eq 1 define the fluxes due to diffusion, electrical migration, and convection, respectively. The electrical potential distribution is governed by the Poisson equation

$$\nabla\cdot(\epsilon_r\nabla\phi) = -\frac{\rho_e}{\epsilon_0} \tag{2}$$

where ϵ_0 is the permittivity of vacuum, ϵ_r is the relative permittivity, and ρ_e is the net charge density of ions. The net charge density is defined by

$$\rho_e = F\sum_{i=1}^{m} z_i c_i \tag{3}$$

where m is the total number of species involved in the system. The material-balance equation or the Nernst−Planck (NP) equation describes the mass transfer of each dissolved species and is given by

$$\frac{\partial c_i}{\partial t} = -\nabla\cdot\Gamma_i \tag{4}$$

In micro- and nanometer channels, the Reynolds number is very low such that the convective terms in the Navier−Stokes equations can be neglected.[34] Therefore, we can solve the Stokes equation and the continuity equation to obtain the velocity distribution. The Stokes equation for the velocity and the continuity equation for the incompressible fluid describe the movement of the fluid through the channels and are given by

$$-\nabla p + \mu\nabla^2\mathbf{u} - \rho_e\nabla\phi = 0 \tag{5}$$

$$\nabla\cdot\mathbf{u} = 0 \tag{6}$$

(22) Qiao, R.; Aluru, N. R. *J. Chem. Phys.* **2003**, *118*, 4692−4701.
(23) Qiao, R.; Aluru, N. R. *Phys. Rev. Lett.* **2004**, *92*, 198301.
(24) Qiao, R.; Aluru, N. R. *Appl. Phys. Lett.* **2005**, *86*, 143105.
(25) Qiao, R.; Aluru, N. R. *Langmuir* **2005**, *21*, 8972−8977.
(26) Qiao, R.; Georgiadis, J. G.; Aluru, N. R. *Nano Lett.* **2006**, *6*, 995−999.
(27) Joseph, S.; Aluru, N. R. *Langmuir* **2006**, *22*, 9041−9051.
(28) Pennathur, S.; Santiago, J. G. *Anal. Chem.* **2005**, *77*, 6772−6781.
(29) Moya, A. A.; Horno, J. *J. Phys. Chem. B* **1999**, *103*, 10791−10799.
(30) Quenneville, E.; Buschmann, M. D. *J. Membrane Sci.* **2005**, *265*, 60−73.
(31) Daifuji, H.; Yang, P.; Majumdar, A. *Nano Lett.* **2004**, *4*, 137−142.
(32) Daifuji, H.; Yang, P.; Szeri, A. J.; Majumdar, A. *Nano Lett.* **2004**, *4*, 2315−2321.
(33) Karniadakis, G. E.; Beskok, A.; Aluru, N. R. *Microflows and Nanoflows: Fundamentals and Simulation*; Springer: New York, 2005.
(34) Mitchell, M. J.; Qiao, R.; Aluru, N. R. *J. Microelectromech. Syst.* **2000**, *9*, 435−449.

In the above equations, p is the hydrostatic pressure, and μ is the fluid viscosity. The third term in eq 5 is the body force acting on the fluid due to the net charge density and the electric field.

The coupled Poisson and the Nernst−Planck equations (PNP) and the Stokes equations are solved using the finite cloud method.[35−39] The computed solutions include the electric potential, ionic concentration, velocity, and pressure profiles in the system. The current through the channel is calculated by integrating the ionic fluxes over the cross-section, i.e.,

$$\mathbf{I} = \int_S \sum_i z_i F \Gamma_i \, dS \tag{7}$$

where S is the cross-sectional area of the channel. Note that the depth (the third dimension) has a unit width which is taken as 1 m in this paper.

3. Micro−Nanofluidic System

To understand the physical phenomena in hybrid micro−nanofluidic systems,[10−13] we consider a canonical problem as shown in Figure 1. The hybrid system consists of a single nanochannel connected to two microchannels. The top microfluidic channel (the ends of which are connected to electrodes 1 and 2) is designated as the source channel, and the bottom microfluidic channel (the ends of which are connected to electrodes 3 and 4) is designated as the receiving channel. The dimensions of the top microchannel and the bottom microchannel are identical. The microchannels have a length of 100 μm and a width of 1 μm. The nanochannel is 1 μm long and 10 nm in width. The currents are measured at the ends of the microchannels.

The system is designed to control the mass transfer between the source channel and the receiving channel through the nanochannel. Typical operation of the hybrid micro−nanofluidic system includes three stages: rest, injection, and recovery. Initially, the system is at the rest stage during which a potential of 40 V is applied on terminal 1, while terminal 2 is grounded, and terminals 3 and 4 are electrically floating. Then the injection is initiated during which ions are transferred from one microchannel to the other. The injection stage lasts for 25 ms. During the injection stage, the source channel is either positively biased relative to the receiving channel or vice versa. Defining the potential bias as

$$\Delta V = V_{\text{receiving}} - V_{\text{source}} \tag{8}$$

we consider two types of biasing, with ΔV being positive or negative. When $\Delta V > 0$, the external electric field is from the receiving channel to the source channel and this is defined as a positively biased case (see Table 1). When $\Delta V < 0$, the external electric field is from the source channel to the receiving channel and this is defined as a negatively biased case (see Table 1). At the end of the injection stage, the applied potentials on the electrodes are reverted back to those of the rest stage, so that the system evolves back to the steady state. A summary of the applied voltage during each stage is given in Table 1.

We perform two-dimensional simulations by assuming that the depth of the micro- and nanochanels is much larger than the width. In the simulations, the reservoirs connected to the microfluidic channels are filled with 1 mM potassium biphosphate (KH_2PO_4). We assume the concentration of H^+ and OH^- is much lower than the bulk concentration. In such a case, the water dissociation is very low and the current is primarily due to the salt ions.[40] Hence, we do not consider the water dissociation effect in this paper. The diffusivities of K^+ and $H_2PO_4^-$ are 1.96×10^{-9} and 0.87×10^{-9} m^2/s, respectively. The ionic concentrations at the ends of the microchannels are given by constant values of 1 mM. The normal flux of each ion is assumed to be zero on channel walls. The dielectric constant of the solution, ϵ_r, is 80. Boundary condition for the electric potential on the channel walls is given by

$$\nabla_\perp \phi = -\frac{\sigma}{\epsilon_0 \epsilon_r} \tag{9}$$

where $\perp$ denotes the wall-normal component, and σ is the surface charge density of channel walls. The surface charge density of the nanochannel is assumed to be $+0.35$ mC/m^2. The surface charge density of the microchannels is assumed to be -0.05 mC/m^2. For the electrically floating boundary condition, the normal gradient of electric potential is assumed to be zero. Nonslip boundary conditions are assumed on the channel walls for the fluid velocities. Continuity eq 6 is enforced on the channel walls. Pressure is assumed to be zero at the ends of the microchannels.

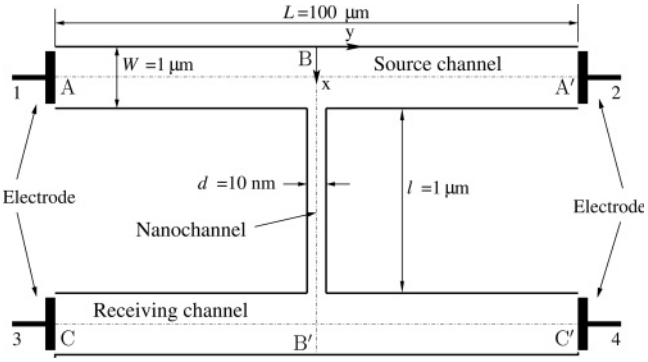

Figure 1. Canonical hybrid micro−nanofluidic system not drawn to scale. Note the position of the origin of the coordinate system and the placement of the x and y axes.

Table 1. Applied Voltages during Rest, Injection, and Recovery Stages

	positively biased				negatively biased			
potential (V)	1	2	3	4	1	2	3	4
rest	40	0	float	float	40	0	float	float
injection	0	0	40	40	40	40	0	0
recovery	40	0	float	float	40	0	float	float

4. Results

In this section, we investigate the ion enrichment−depletion phenomena at the micro−nanofluidic junction regions and the unique current signatures resulting from it by studying the ionic concentration and potential variation in the microchannel and the nanochannel. The convective flow field associated with the phenomena is also investigated. The simulations are performed in three stages as outlined in Table 1. First, we simulate the time independent rest stage where the electrolyte moves between electrodes 1 and 2 in the source channel. Second, time-dependent injection stage using the rest stage as the initial condition is simulated. In this stage, the accumulation and depletion of ions is observed at the micro−nano junction regions. After 25 ms of injection, the electrode potentials are switched back to the rest stage potentials to observe the time dependent recovery stage at the end of which the device is back at the rest stage. We plot the concentration profiles, potential profiles, current signatures, and electroosmotic velocities to study the ion enrichment−depletion phenomena.

4.1. Accumulation and Depletion of Ions. Typically, in experiments of micro−nano hybrid preconcentration devices,[7,41]

(35) Aluru, N. R. *Int. J. Numer. Methods Eng.* **2000** *47*, 1083−1121.
(36) Aluru, N. R.; Li, G. *Int. J. Numer. Methods Eng.* **2001**, *50*, 2373−2410.
(37) Jin, X.; Li, G.; Aluru, N. R. *Comput. Model. Eng. Sci.* **2001**, *2*, 447−462.
(38) Jin, X.; Li, G.; Aluru, N. R. *Comput. Methods Appl. Methods Eng.* **2004**, *193*, 1171−1202.
(39) Jin, X.; Li, G.; Aluru, N. R. *Comput. Struct.* **2005**, *83*, 1366−1385.
(40) Krol, J.; Wessling, J. M.; Strathmann, H. *J. Membr. Sci.* **1999**, *162*, 145−154.

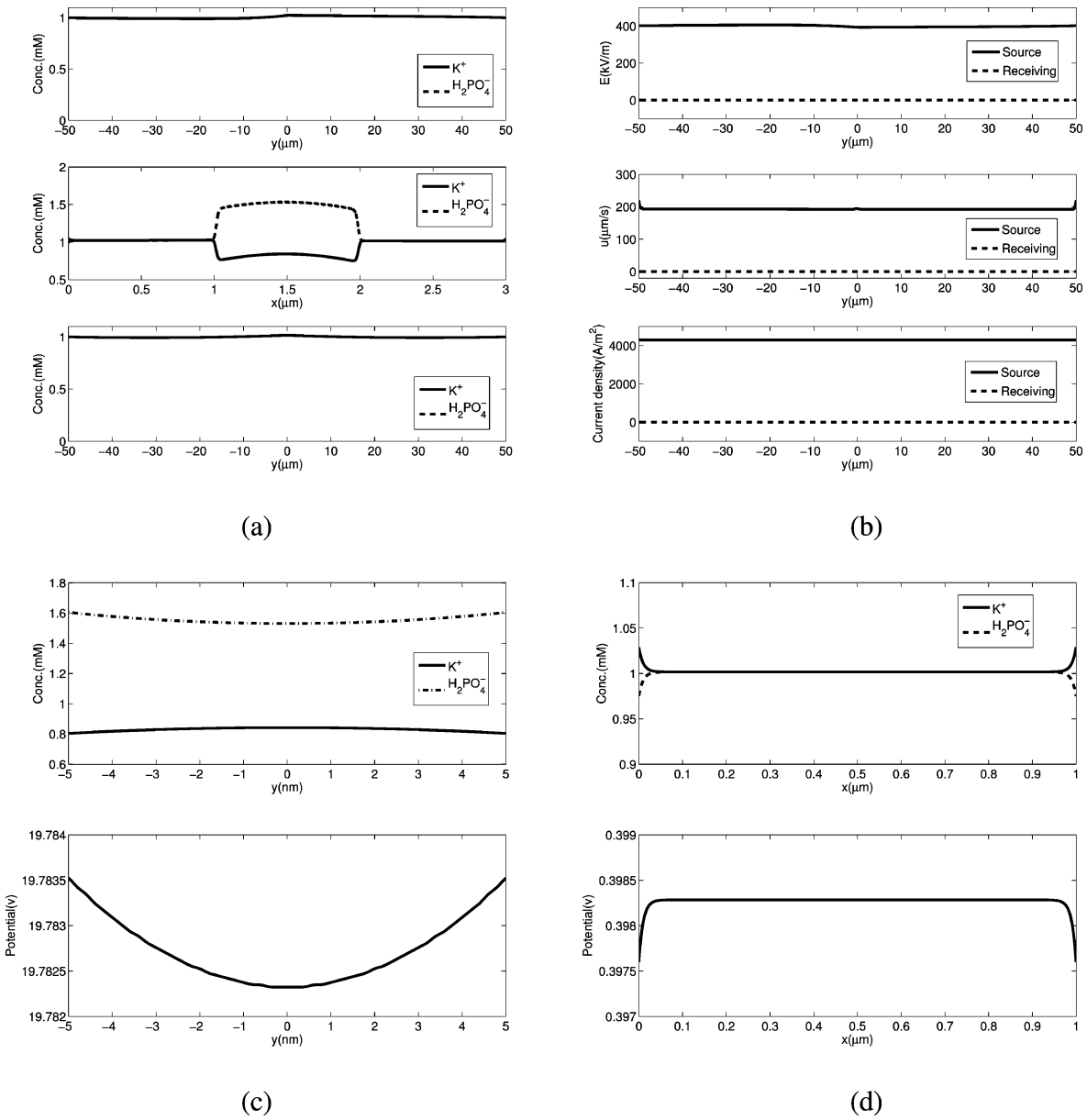

Figure 2. (a) Ionic concentrations in the rest stage. Top: Ionic concentrations along the central line *AA′* (see Figure 1) of the source channel. Note that the anion and cation concentrations are the same in both the source and the receiving channel. Middle: Ionic concentrations along the line *BB′*. Bottom: Ionic concentrations along the central line *CC′* of the receiving channel. (b) The electric field, velocity, and current density in the source and receiving channel. Top: electric field along the central lines *AA′* and *CC′*. Middle: fluid velocity along the central lines *AA′* and *CC′*. Bottom: current density along the central lines *AA′* and *CC′*. (c) Ionic concentrations and potential across the nanochannel at $x = 1.5\ \mu$m. Top: cation and anion concentrations. Bottom: electric potential. (d) Ionic concentrations and potential across the microchannel at $y = 45\ \mu$m. Top: cation and anion concentrations. Bottom: electric potential.

electric fields are applied along the nanochannel. Depending on the magnitude and direction of the electric field, phenomena such as depletion/enrichment or preconcentration of analytes are observed. We simulate the rest stage first which is a steady-state condition where voltages are applied only at the ends of source channel and then switch the electrode potentials to the injection stage where voltages are applied at the ends of both the source and the receiving channel. In the simulations, the nanochannel is assumed to have a fixed positive surface charge and the microchannels are assumed to have a fixed negative surface charge.

In the rest stage, electrodes 1 and 2 have a potential difference of 40 V between them, and electrodes 3 and 4 are floating, as shown in Table 1. We solve the steady-state PNP and Stokes equations to obtain the concentration and electrical potential profiles before the injection begins. Figure 2a shows the concentrations of cations and anions in the microchannels and the nanochannel, and Figure 2b shows the electric field, fluid velocity, and current in the microchannels. Since the receiving channel is electrically floating, the electric field in the receiving channel (see Figure 2b (top)) is almost zero, and consequently, there is no ionic migration or electroosmotic flow in the receiving channel (see Figure 2b (middle)), and no current in the receiving channel (see Figure 2b (bottom)).

From Figure 2a, we note that the anion and cation concentrations are the same in the source and receiving channels, but the nanochannel anion concentrations are higher than the bulk with cations being depleted. The Debye length at a concentration of

(41) Kim, S. M.; Burns, M. A.; Hasselbrink, E. F. *Anal. Chem.* **2006**, *78*, 4779−4785.

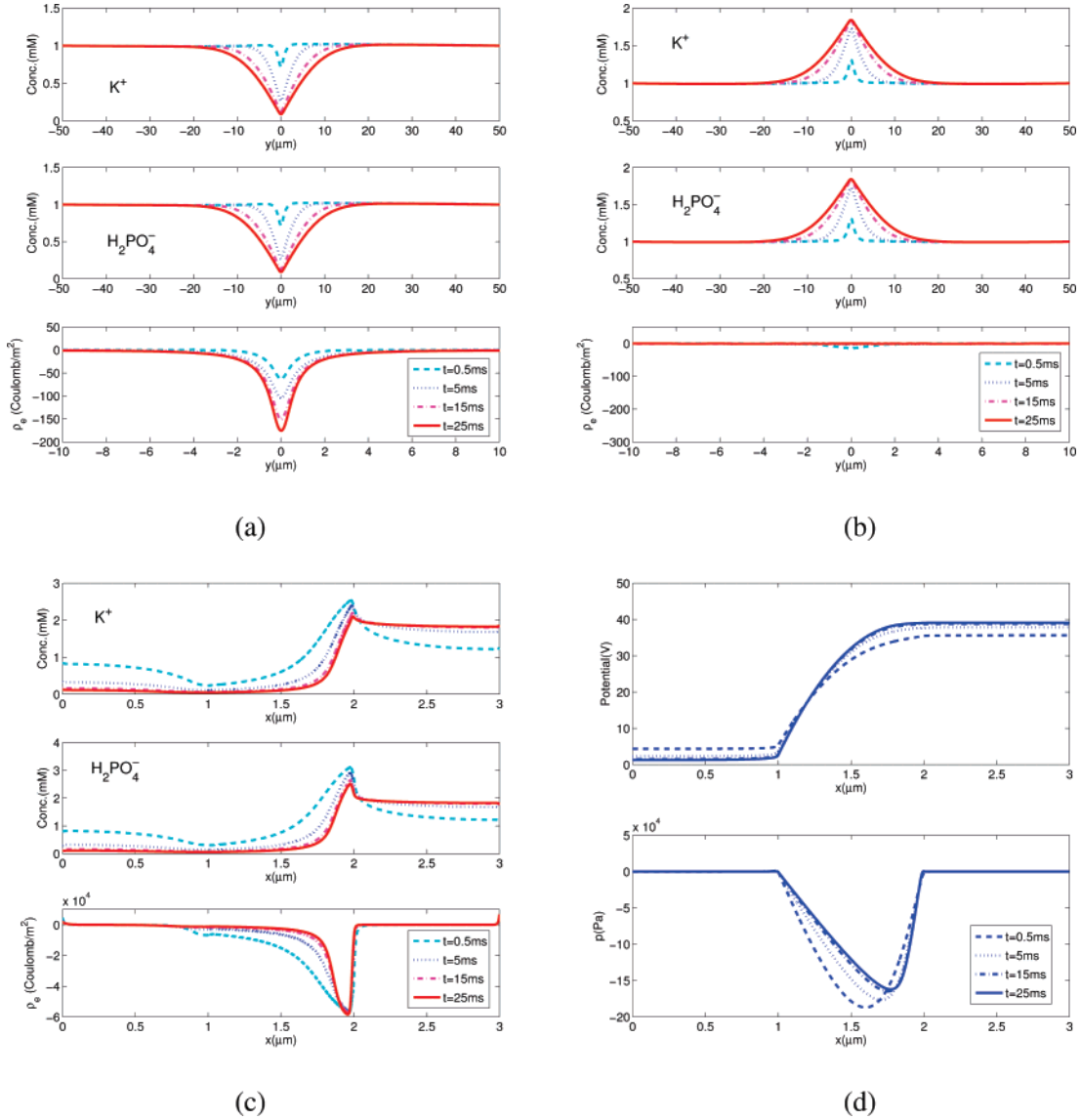

Figure 3. Simulation of the injection stage with $\Delta V = 40$ V potential bias: (a) Ionic concentrations along the central line AA' of the source channel. Top: cation concentration. Middle: anion concentration. Bottom: the space charge density. (b) Ionic concentrations along the central line CC' of the receiving channel. Top: cation concentration. Middle: anion concentration. Bottom: the space charge density. (c) Ionic concentrations along the central line BB' of the nanochannel. Top: cation concentration. Middle: anion concentration. Bottom: the space charge density. (d) Variation of potential and pressure along the central line BB' of the nanochannel. Top: electric potential. Bottom: pressure.

1 mM is about 10 nm ($\kappa^{-1} = 0.308c^{-1/2} = 9.74$ nm).[42] The electric double layer in the microchannel is a small portion of the microchannel, so that the anion and cation concentrations are the same at the center, as shown in Figure 2d. However, the electrical double layers in the nanochannel overlap, as illustrated by the cross-sectional distributions of the ionic concentrations and potential in the nanochannel in Figure 2c. This leads to an increase in anions and decrease in cations in the nanochannel since the surface of the nanochannel is positively charged. The difference in ion concentration between cations and anions is determined by the surface charge density. From the electroneutrality requirement, the difference in ionic concentration in the nanochannel is given by

$$\int (c_1 - c_2)\, dy = -\frac{2\sigma}{Fd} \qquad (10)$$

where c_1 and c_2 are the concentrations of cations and anions, respectively, σ is the surface charge of the nanochannel, which is $+0.35$ mC/m^2, and d is the width of the nanochannel, which is 10 nm. From eq 10, the difference between the cation and anion concentration is -0.725 mM. From Figure 2c (top), the concentration difference between the cation and anion is also -0.725 mM, which indicates that the electroneutrality condition is satisfied in the nanochannel during the rest stage.

Using the concentrations and potentials of the rest stage as initial conditions, we performed transient simulations for the injection stage. We define two types of injections depending on the direction of the flux in the nanochannel or the applied potential bias between the source channel and the receiving channel as shown in Table 1. Since the physical phenomena of ionic transport is the same in both cases, we discuss in detail only the positively biased case.

For the positively biased case ($\Delta V > 0$), from Figure 3a, b, and c, we observe that (i) both cations and anions initially deplete at the source−nanochannel junction region and the depletion region spreads to as wide as 40 μm by the time, $t = 25$ ms, (ii) both cations and anions accumulate in the receiving channel with a similar accumulation region width, (iii) a net space charge

(42) Delgado, A. V; Arroyo, F. J. *Interfacial Electrokinetics and Electrophoresis*; Delgado, A. V., Ed.; Marcel Dekker, Inc.: New York, 2002.

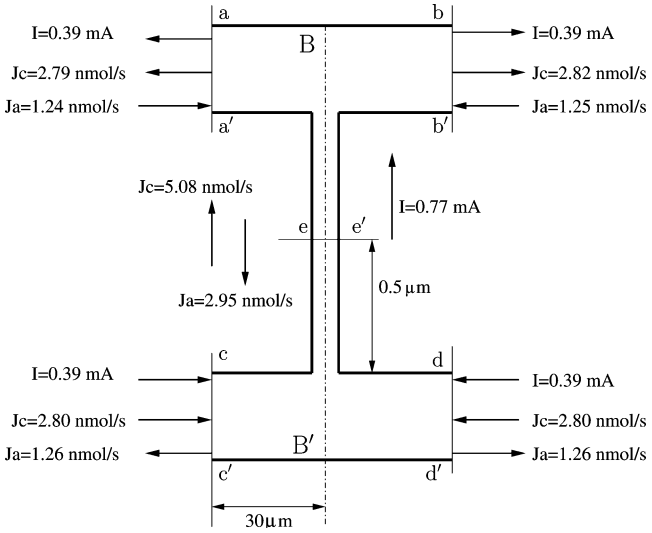

Figure 4. Cross-sectional fluxes for cations and anions and the total current during the injection stage at $t = 7.5$ ms. The cross-sectional fluxes are defined as $\mathbf{J}_i = \int_S \Gamma_i \, dS$ and the units are in nmol/s. J_a and J_c refer to the anion and cation cross-sectional fluxes, respectively. The current I is defined in eq 7 with the units in mA.

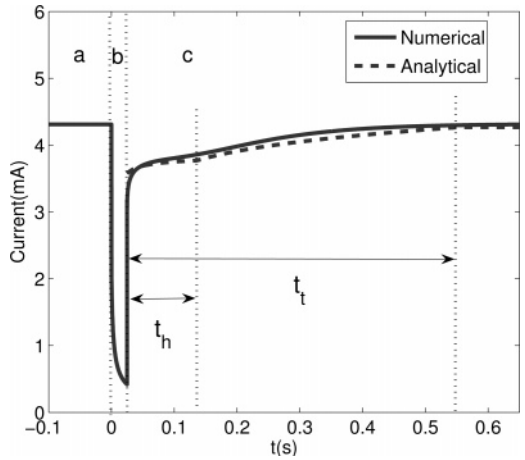

Figure 5. Ionic current in the source channel vs time when the system is positively biased. (a) current during the rest stage, (b) current during the injection stage, and (c) current during the recovery stage. The analytical solution is calculated from eq 16. t_h and t_t can be estimated from eqs 21 and 22, respectively.

density as defined in eq 3 is developed in the source microchannel, (see Figure 3a (bottom)), but the receiving channel is electrically neutral (see Figure 3b (bottom)), and (iv) in the nanochannel, there is an ion depletion at the end connected to the source channel, and an ion accumulation, at the end connected to the receiving channel.

In order to understand the accumulation and depletion at the micro−nano junction regions, we examine the cation and anion fluxes during the injection at $t = 7.5$ ms which is shown schematically in Figure 4. With positive potentials at the ends of the receiving channel, the cations tend to move from the reservoirs of the receiving channel to the reservoirs of the source channel. The anions tend to move from the reservoirs of the source channel to the reservoirs of the receiving channel through the nanochannel. The net cation flux from the ends of the receiving microchannel to the receiving−nanochannel junction is larger than the cation flux from the junction through the nanochannel because cations are repelled by the positively charged nanochannel. The difference between the fluxes causes the accumulation of cations in the receiving−nanochannel junction region. The

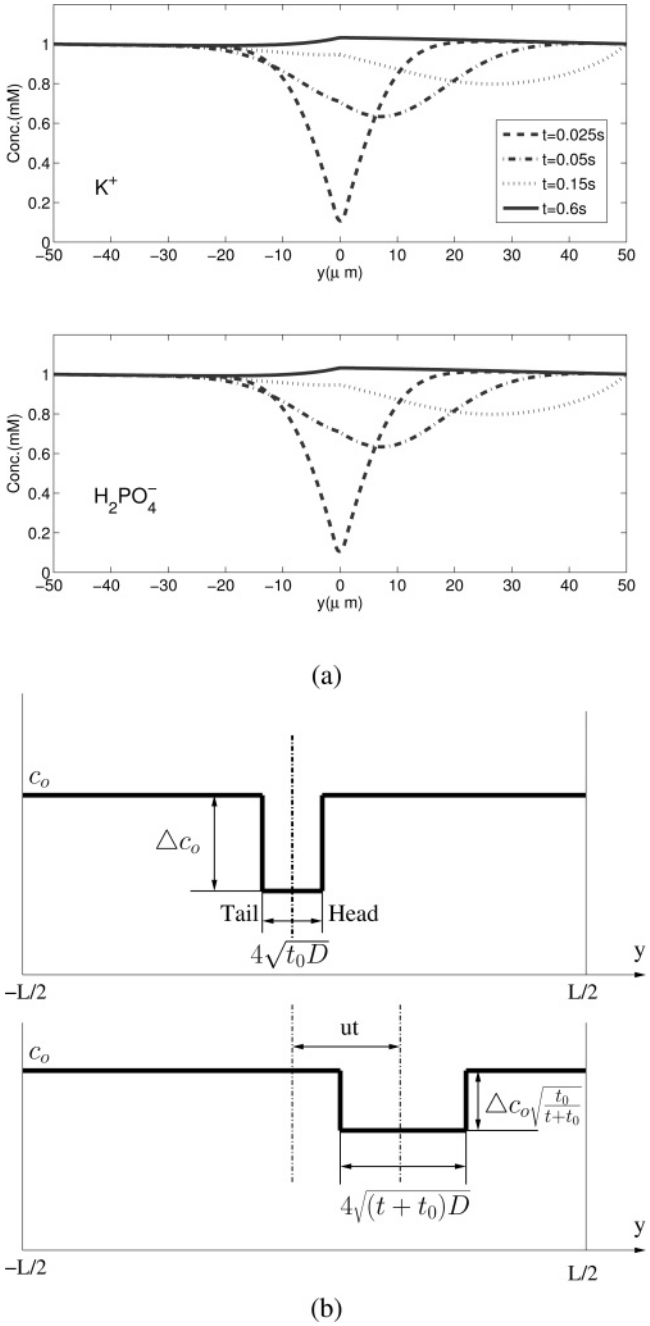

Figure 6. (a) Ion concentration along the central line of the source channel during the recovery stage. Note that the recovery stage starts from $t = 0.025$ s. (Top) cation concentration. (Bottom) anion concentration. (b) A simplified model for the treatment of depletion in the source channel. (Top) approximation of the depletion region at the beginning of the recovery stage. (Bottom) approximation of the depletion region at time t.

anion flux from the nanochannel into the receiving channel is greater than that from the receiving channel to the reservoir, because some anions from the nanochannel remain in the junction region to balance the accumulated cations, causing an accumulation of anions as well in the receiving channel. On the other hand, at the source−nanochannel junction, the cation flux from the nanochannel is not sufficient to balance the cation flux from the source channel to the reservoirs due to limited cations passing through the nanochannel. This causes a depletion of cations in the source−nanochannel junction region. Meanwhile, the anion flux from the reservoirs to the source−nanochannel junction is less than the anion flux into the nanochannel because the anions

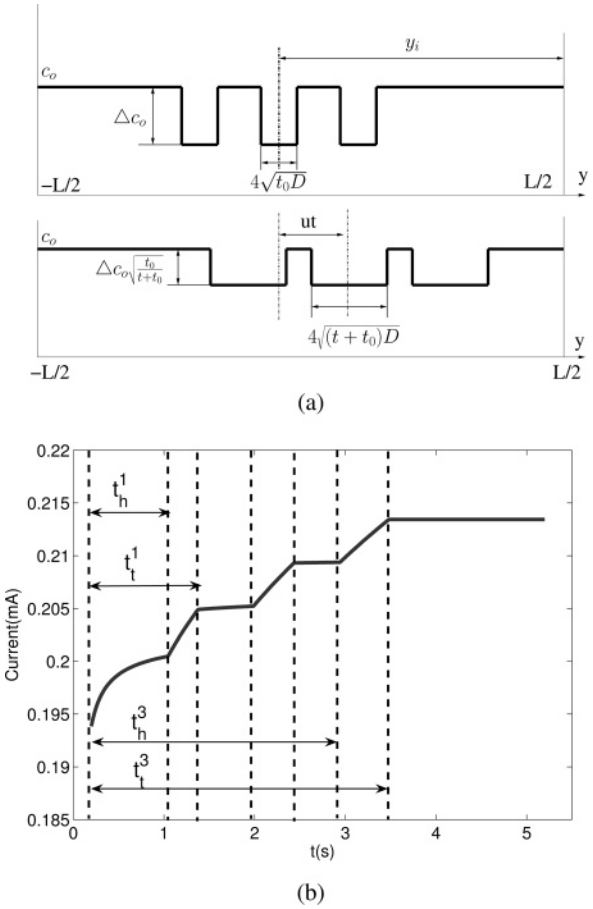

Figure 7. (a) Schematic of multiple depletion regions in the microchannel (Top) ionic concentration at the beginning. (Bottom) ionic concentration at time *t*. (b) Ionic current obtained using eq 23.

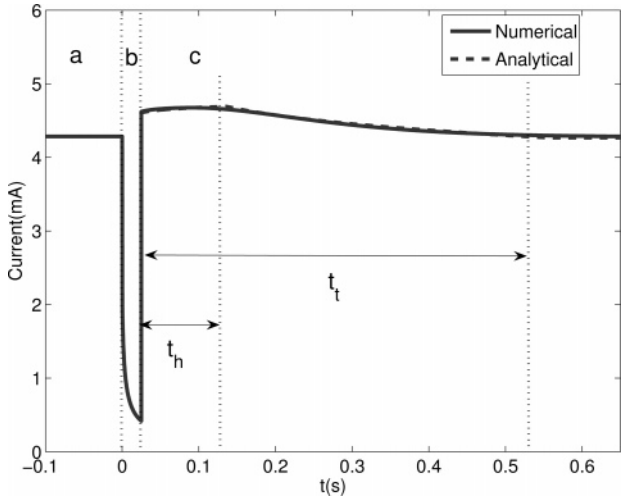

Figure 8. Ionic current in the source channel vs time for the negatively biased case. (a) current in the rest stage, (b) current during the injection stage, and (c) current during the recovery stage. The analytical solution is calculated from eqn. (16). t_h and t_t can be estimated from eqs 21 and 22, respectively.

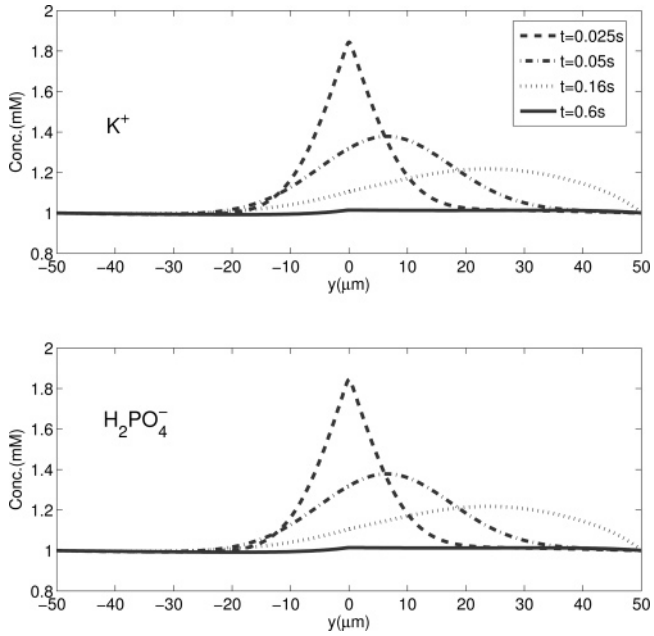

Figure 9. Ion concentration along the central line of the source channel during the recovery stage when the system is negatively biased. Note that the recovery stage starts from $t = 0.025$ s.

are attracted by the positively charged nanochannel. The difference results in a depletion of anions in the top junction. Thus, both anions and cations are depleted in the junction of the source channel and the nanochannel, while both anions and cations accumulate in the junction of the receiving channel and the nanochannel. According to the Gouy−Chapman model,[42] the double-layer thickness is inversely proportional to the square root of the electrolyte concentration. Because the ion concentration is extremely low due to depletion in the source−nanochannel junction, the electrical double layer extends into the source channel with a higher anion concentration than the cation concentration such that there is a region of induced space charge in the source channel. In contrast, in the receiving channel, with the ionic concentrations being much higher, the Debye length is much smaller and there is no net space charge observed in the receiving channel. In the source channel, the space charge increases as time progresses and spreads to a wider region.

The accumulation−depletion phenomena in microchannels also affect the concentration of ions in the nanochannel. Figure 3c shows the ionic concentration profiles in the nanochannel. As injection progresses, the depletion region in the source channel extends into the end of the nanochannel connected to the source channel and the space charge in this part of the nanochannel is not sufficient to neutralize the surface charge (see Figure 3c (bottom)). However, at the other end of the nanochannel connected to the receiving channel, the accumulation in the receiving channel causes the ionic concentrations to increase, but still maintaining sufficient space charge to neutralize the positively charged nanochannel surface. In the depletion region of the nanochannel ($1.0 < x < 1.9$ μm), the potential increases sharply, as shown in Figure 3d (top). The change in the net space charge in the region $1.0 < x < 1.9$ μm results in an increase of the electroosmotic driving force along the nanochannel. This induces a pressure drop in the region $1.0 < x < 1.9$ μm (see Figure 3d (bottom)), so that the fluid flow is continuous.

If the electric field in the nanochannel is reversed, i.e., the potential bias is negative ($\Delta V < 0$), the depletion occurs in the receiving channel and the accumulation in the source channel. The ion-enrichment and ion-depletion mechanism is the basis of the concept of molecular gates which can be used to concentrate dilute analyte solutions or remove high salt components from a sample.[11]

4.2. Ionic Currents. In the previous section we explained how injection of the fluid from one microchannel to another microchannel results in ion accumulation−depletion in the junction regions. In this section, we compute the ion currents and discuss how the accumulation−depletion affect the currents

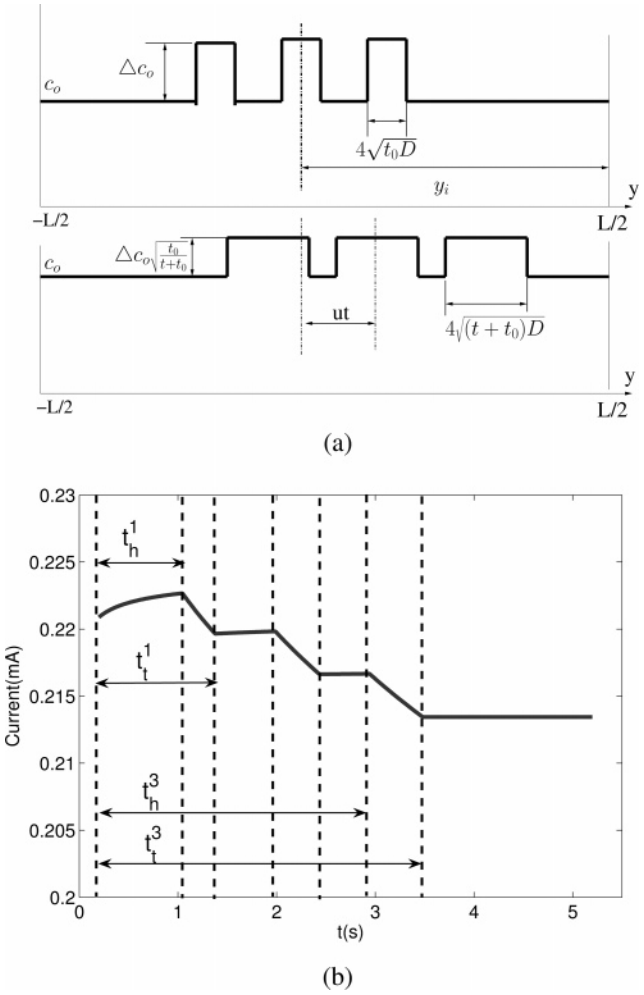

Figure 10. (a) Schematic of multiple accumulation regions in the microchannel (Top) ionic concentration at the beginning. (Bottom) ionic concentration at time *t*. (b) Ionic current obtained using eq 23.

during the rest, injection and recovery stages. The ionic current is calculated using eq 7 at the ends of the source channel where electrical potentials are applied. In the rest and recovery stages, the ionic currents are measured at terminal 1, while in the injection stage, the ionic current is the summation of the currents measured at both terminal 1 and terminal 2.

Figure 5 shows the transient variation of the ionic current during the rest, injection and recovery stages when the system is positively biased (see Table 1). The current signature shows that (i) when the injection is turned on, the current drops to less than 10% of the rest current within 25 ms of injection, and (ii) during the recovery stage, the current initially increases rapidly, reaches a plateau, before a gradual increase to the steady-state value.

During the injection stage at positive bias, ions deplete in the source−nano junction and accumulate in the receiving−nano junction, resulting in a rapid increase of potential difference between the ends of the nanochannel (see Figure 3d (top)). Depletion also results in an increase of electrical resistance in the source−nano junction, while accumulation results in a decrease of resistance in the receiving−nano junction. However, the depletion has a disproportionate effect on the resistance compared to the accumulation because the resistance is inversely proportional to the ionic concentration. Thus, the overall resistance in the system increases, causing the ionic current to decrease.

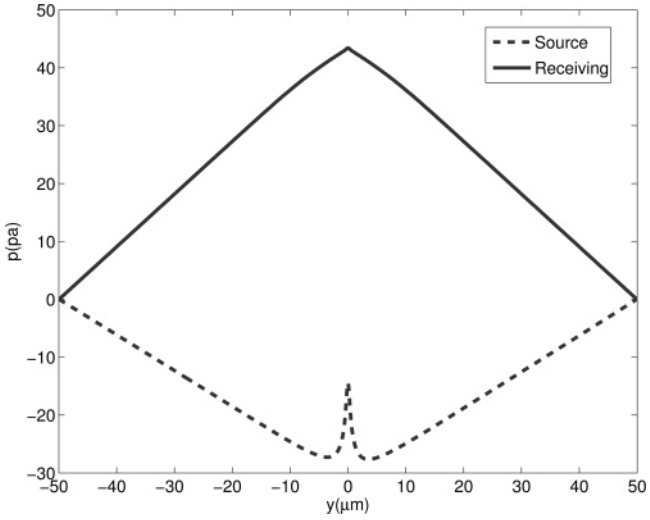

Figure 11. Pressure profiles along the center line of source channel and receiving channel during the injection stage (at $t = 15$ ms).

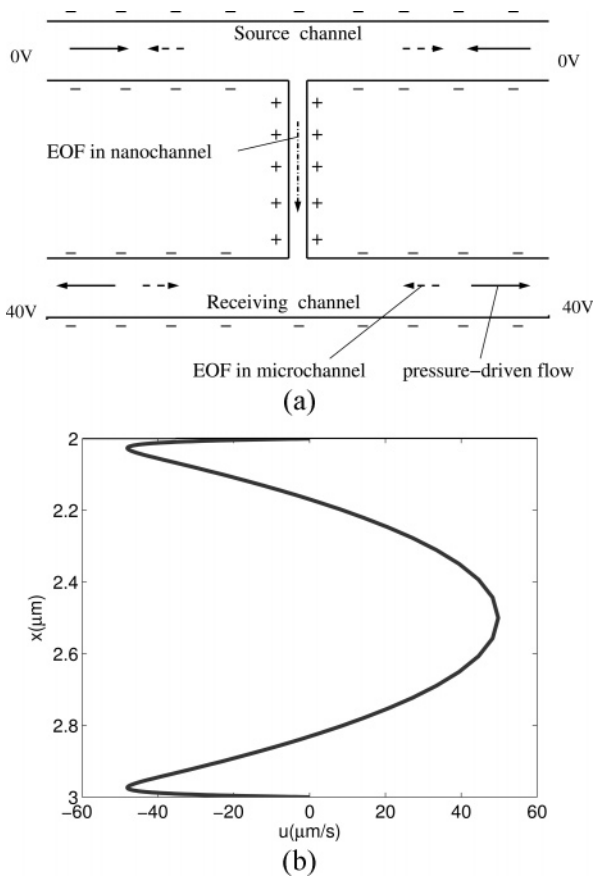

Figure 12. Electroosmotic flow (EOF) during the injection stage when the receiving channel is positively biased relative to the source channel. (a) Schematic diagram indicating the direction of electroosmotic flow and induced pressure-driven flow in the system. (b) Velocity profile across the receiving channel near the reservoir (at $t = 15$ ms, $y = 45$ μm).

At $t = 25$ ms, when the electrode potentials are switched to revert the system back to the rest state, two key features are observed. (i) The depletion region moves out of the source channel, as shown in Figure 6, due to the fluid flow in the source channel and (ii) the depletion region broadens to a wider region due to diffusion. The current measured at the end of the source channel (at $y = -L/2$) is affected by the depletion of ions in the source channel. This can be easily understood by

considering a 1D form of eqs 1 and 4. Assuming the concentrations of the anions and the cations to be the same, from eqs 1 and 4 we obtain

$$-(D_1 - D_2)\frac{\partial^2 c}{\partial y^2} = (\Omega_1 + \Omega_2)F\frac{\partial}{\partial y}\left(c\frac{\partial \phi}{\partial y}\right) \tag{11}$$

where D_1 and D_2 are the diffusion coefficients of cations and anions, respectively. $\Omega_1$and Ω_2 are the mobilities of cations and anions, respectively. Integrating from $-L/2$ to y, with the condition that there is no concentration gradient in the reservoir at $y = -L/2$, we obtain

$$(\Omega_1 + \Omega_2)F\frac{\partial \phi}{\partial y} = (\Omega_1 + \Omega_2)F\left.\frac{\partial \phi}{\partial y}\right|_{y=-L/2}\frac{c_0}{c(y)} - \frac{(D_1 - D_2)}{c(y)}\frac{\partial c}{\partial y} \tag{12}$$

where c_0 is the ionic concentration at $y = -L/2$. Integrating from $y = -L/2$ to $y = L/2$ and using the fact that the concentrations at the ends are the same, the above equation reduces to

$$\left.\frac{\partial \phi}{\partial y}\right|_{y=-L/2}\int_{-L/2}^{L/2}\frac{c_0}{c(y)}\,\mathrm{d}y = \phi_2 - \phi_1 \tag{13}$$

where ϕ_1 and ϕ_2 are the potentials at electrodes 1 and 2. The current at $y = -L/2$ can be obtained from the cation and anion fluxes, i.e.,

$$I|_{y=-L/2} = -(\Omega_1 + \Omega_2)F^2 W c_0\left.\frac{\partial \phi}{\partial y}\right|_{y=-L/2} \tag{14}$$

where W is the width of the microchannel. Substituting eq 13 into eq 14, we obtain the current measured at $y = -L/2$

$$I|_{y=-L/2} = -(\Omega_1 + \Omega_2)F^2 W\frac{\phi_2 - \phi_1}{\int_{-L/2}^{L/2}\frac{1}{c(y)}\,\mathrm{d}y} \tag{15}$$

A simple analytical expression for the current arising from the two key features of diffusion of the depletion region and the migration of the depletion region can be obtained from the above equation by assuming an initial concentration profile with a rectangular depletion region at the center of the source channel (see Figure 6b). The reservoir and source channel has a concentration of c_0 except at the depletion region in the center that has a width of $4\sqrt{t_0 D}$ and a concentration of $c_0 - \Delta c_0$ initially. D is the pseudo diffusion coefficient of the depletion region and t_0 is the duration of injection. On the basis of the solution of the one-dimensional diffusion equation,[43] we assume that the width of the depletion region changes to $4\sqrt{(t+t_0)D}$ at time t after the beginning of the recovery and the concentration of the depletion region becomes $c_0 - \Delta c_0\sqrt{t_0/(t+t_0)}$, with the area of the depletion region remaining constant. The schematic for the concentration profile variation along the source channel is shown in Figure 6b. For such a variation of the concentration profile with time, the ionic current at time t can be derived from eq 15 as

$$I|_{y=-L/2} = \frac{I_\infty}{1 + g(t)w(t)} \tag{16}$$

where I_∞ is the ionic current at the steady-state,

$$I_\infty = \frac{(\Omega_1 + \Omega_2)F^2 W(\phi_1 - \phi_2)c_0}{L} \tag{17}$$

and

$$g(t) = \frac{1}{\sqrt{\frac{t + t_0}{t_0}\frac{c_0}{\Delta c_0} - 1}} \tag{18}$$

and

$$w(t) = \begin{cases} 4\sqrt{(t + t_0)D}/L & \text{if } ut + 2\sqrt{(t + t_0)D} \le L/2 \\ 1/2 + 2\sqrt{(t + t_0)D}/L - ut/L & \text{if } -2\sqrt{(t + t_0)D} < ut - L/2 < 2\sqrt{(t + t_0)D} \\ 0 & \text{if } -2\sqrt{(t + t_0)D} \ge L/2 \end{cases} \tag{19}$$

where u is the convective velocity. The velocity can be estimated by[34]

$$u = \frac{(\phi_2 - \phi_1)\zeta\epsilon_r\epsilon_0}{L\mu} \tag{20}$$

where ζ is the zeta-potential on the microchannel wall. When the depletion region remains in the source channel, i.e., if $ut + 2\sqrt{(t+t_0)D} < L/2$, the ionic current increases rapidly at the beginning and then reaches a plateau as the depletion region becomes flat in the source channel. However, at the time when $ut + 2\sqrt{(t+t_0)D} = L/2$, the head of the depletion region touches the end of the source channel and the depletion region starts to move out of the source channel. The ionic current increases gradually as the depletion region starts to move out. When $ut - 2\sqrt{(t+t_0)D} > L/2$, the tail of the depletion region reaches the end of the source channel and the ionic current remains a constant after this time. Let us define t_h as the time when the head of the depletion region reaches the end of the microchannel, and t_t is the time when the tail touches the end of the microchannel. If the length of the microchannel is much larger than the width of the depletion region, t_h can be approximated by

$$t_h \approx \frac{L/2 - 2\sqrt{\left(t_0 + \frac{L}{2u}\right)D}}{u} \tag{21}$$

and t_t can be approximated by

$$t_t \approx \frac{L/2 + 2\sqrt{\left(t_0 + \frac{L}{2u}\right)D}}{u} \tag{22}$$

The comparison of the ionic current in the recovery stage calculated from eq 16 and that from simulations gives a good match as seen in Figure 5. In the calculation using the analytical expression, the initial depletion region from the simulation (see Figure 6a (top)) was approximated by a rectangular depletion region with $\Delta c_0 = 0.45$ mM. The injection time t_0 equals 0.025 s. The diffusion coefficient is chosen to be the average of the diffusion coefficient of the anion and the cation. The bulk concentration c_0 is 1 mM. The velocity is 0.2 mm/s, using $\zeta = -0.7$ mV (from Figure 2d (bottom)). The head of the depletion region touches the end of the microchannel at approximately $t_h = 0.11$ s after the beginning of the recovery, and the tail of the depletion region reaches the end of the microchannel at approximately $t_t = 0.53$ s.

Multiple ion depletions in hybrid micro−nano devices with several nanochannels can give rise to interesting features in ionic currents such that these devices could be used as potential logic devices. Consider a scenario with multiple depletion regions in the source channel arising from several micro−nano junctions in the system. Using the analytical equation for current derived above, we investigate the current vs time for such a system with three depletion regions, as shown in Figure 7a. Initially, each depletion region has a width of $4\sqrt{t_0 D}$ and a concentration of $c_0 - \Delta c_0$, and the distance from the center of the ith depletion region to the end of the microchannel is y_i. If the distances between the depletion regions are far enough that they do not overlap with each other during the recovery stage, at time t, the width of the depletion region changes to $4\sqrt{(t+t_0)D}$, and the concentration of the depletion region becomes $c_0 - \Delta c_0\sqrt{(t_0/t+t_0)}$. The electric current at $y = -L/2$ at time t is

$$I(t)|_{y=-L/2} = \frac{I_\infty}{1 + \sum_{i=1}^{n} g(t) w_i(t)} \tag{23}$$

where n is the total number of depletion regions, I_∞ is given by eq 17, $g(t)$ is given by eq 18, and $w_i(t)$ defines the width of the ith depletion region remaining in the microchannel:

$$w_i(t) = \begin{cases} 4\sqrt{(t+t_0)D}/L & \text{if } ut + 2\sqrt{(t+t_0)D} \le y_i \\ y_i/L + 2\sqrt{(t+t_0)D}/L - ut/L & \text{if } -2\sqrt{(t+t_0)D} < ut - y_i < 2\sqrt{(t+t_0)D} \\ 0 & \text{if } ut - 2\sqrt{(t+t_0)D} \ge y_i \end{cases} \tag{24}$$

Similarly we can estimate the time scales when the head and tail of each depletion region touch the end of the microchannel. The time t_h^i when the head of the ith depletion region reaches the end of the microchannel can be approximated as

$$t_h^i \approx \frac{y_i - 2\sqrt{\left(t_0 + \frac{y_i}{u}\right)D}}{u} \tag{25}$$

and the time t_t^i when the tail of the ith depletion region touches the end of the microchannel can be approximated as

$$t_t^i \approx \frac{y_i + 2\sqrt{\left(t_0 + \frac{y_i}{u}\right)D}}{u} \tag{26}$$

Let us consider a case with three depletion regions. The length of the microchannel is 2 mm. The distances from the center of the depletion regions to the end are 0.5, 1, and 1.5 mm. We assume $\Delta c_0 = 0.5$ mM, $t_0 = 0.2$ s, and $u = 0.5$ mm/s. The electric current

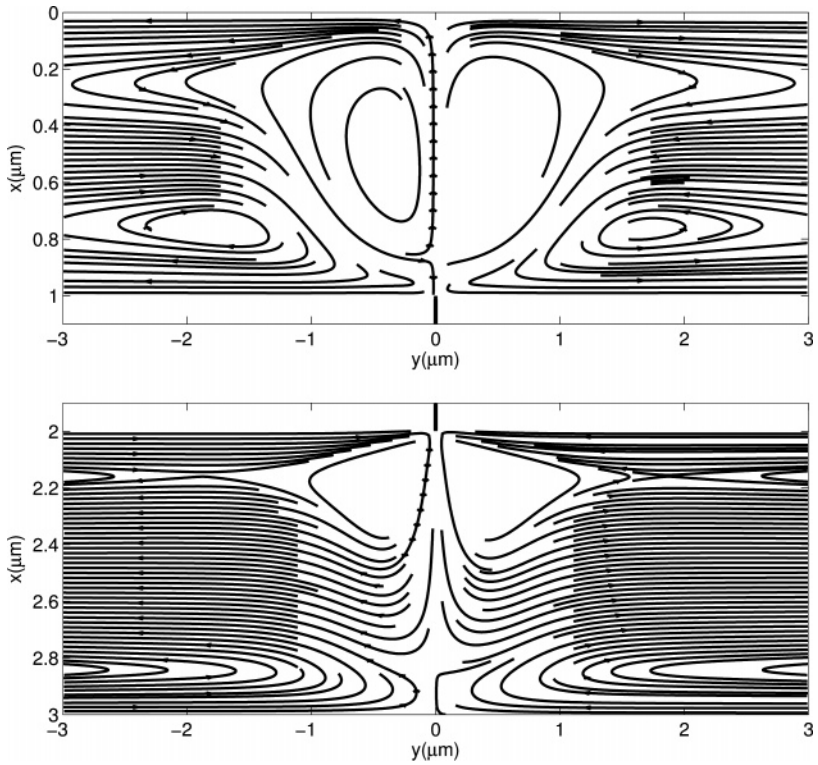

Figure 13. Streamlines (at $t = 15$ ms) near the micro−nano junction regions showing the vortices developed due to opposing electroosmotic and pressure driven flows in the microchannel. Top: near the junction of the source channel and the nanochannel. Bottom: near the junction of the receiving channel and the nanochannel.

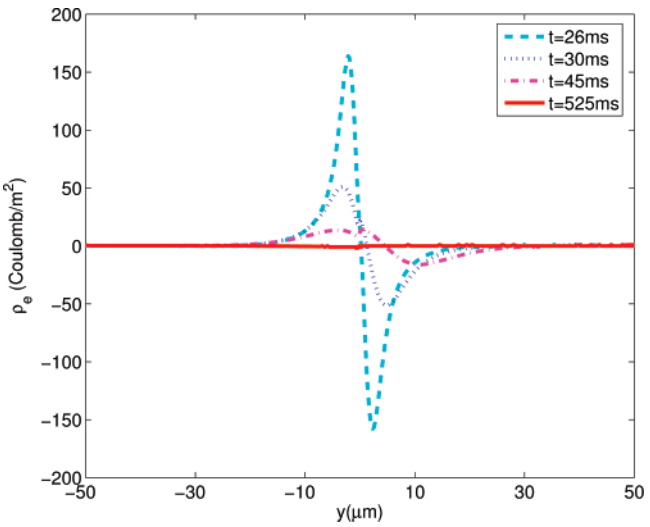

Figure 14. Net charge density along the center line of the source channel during the recovery stage.

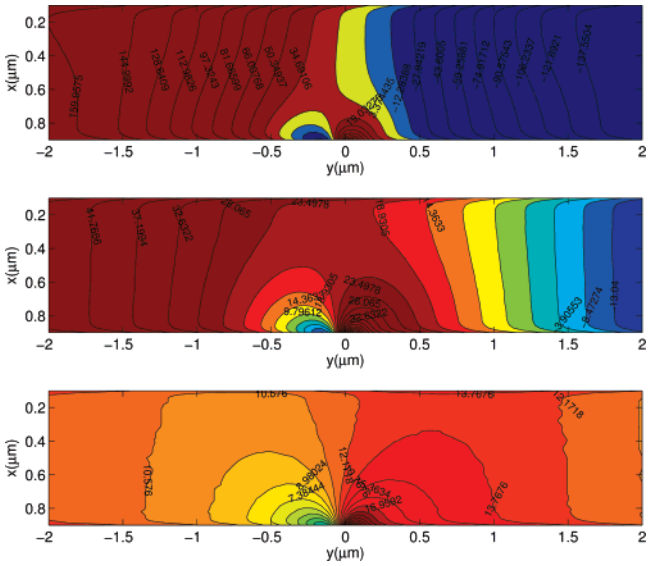

Figure 15. Contours of the space charge density near the source-nanochannel junction region during the recovery stage. Top: at $t =$ 26 ms. Middle: at $t = 30$ ms. Bottom: at $t = 45$ ms.

calculated from eq 23 shows multiple current jumps as the depletion regions move out of the microchannel (Figure 7b). The time scales of the current jumps, t_h^i and t_t^i, shown in the figure are given in eqs 25 and 26.

If the direction of injection is reversed by applying a negative potential bias (see Table 1), the ionic current signature in the source channel is quite different. Figure 8 shows the transient variation of the ionic current during the rest, injection and recovery stages. We observe that (i) during the injection, the current also drops dramatically, similar to the observation in the positively biased case, and (ii) during the recovery stage, the current remains at a higher value than the steady-state current for some time, before gradually decreasing to the steady-state value. In the injection stage, the ions deplete in the junction of receiving and nanochannel, which significantly reduces the ionic conductance in the system. Similar to the positively biased case, there is a sharp potential drop in the nanochannel. Both factors cause the ionic current to drop dramatically in the injection stage. But when the electrode potentials are switched back to the recovery state, the ion-accumulation region moves toward the end of the source channel, as shown in Figure 9. When the accumulation region still remains in the source channel, the conductance in the source channel remains at a higher value, but as the accumulation region passes through the end of the source channel, the ionic

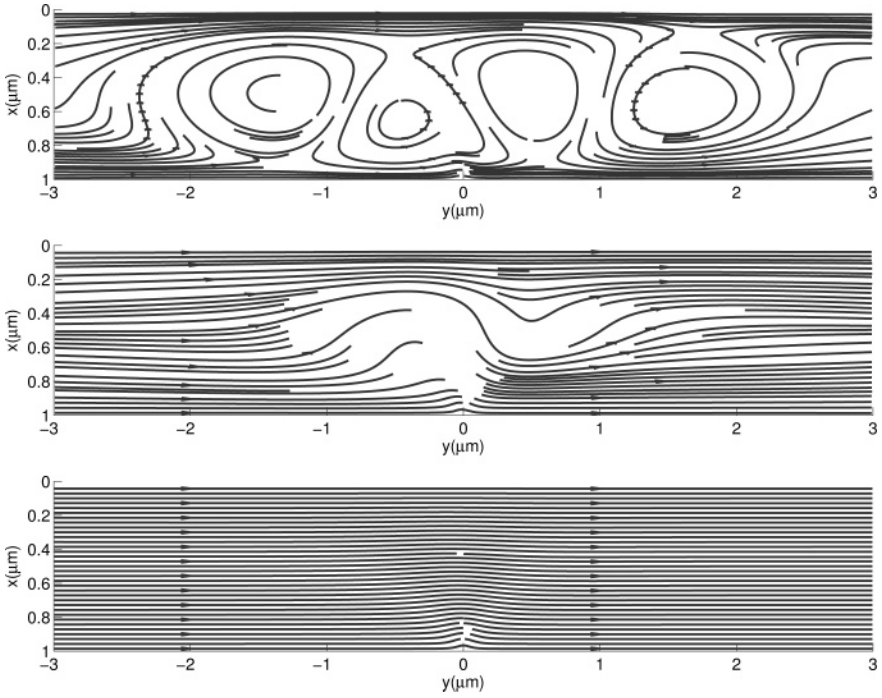

Figure 16. Streamlines near the source-nanochannel junction region during the recovery stage. Top: at $t = 26$ ms. Middle: at $t = 30$ ms. Bottom: at $t = 525$ ms.

concentration decreases, thereby decreasing the conductance and the current decreases to the steady-state value. We can also use eqs 16 and 23 to calculate the electric current at $y = -L/2$ for a single accumulation region and for multiple accumulation regions, respectively. For a single accumulation region in the source channel, Figure 8 shows that the analytical solution captures the trend of the electric current in the recovery stage reasonably well, by using the same parameters as in the single depletion case, except $\Delta c_0 = -0.45$ mM. We also investigated how the electric current changes with time when three accumulation regions are present in the microchannel, as shown in Figure 10a. The current is calculated by using eq 23, with the same parameters as in the case of three depletion regions, except $\Delta c_0 = -0.5$ mM. The electric current in Figure 10b shows multiple current jumps while the accumulation regions move out of the microchannel. The multiple current jumps phenomenon is similar to the staircase signal that can be used to design a multistate memory unit.[44]

4.3. Induced Flow. In this section, we first investigate electroosmotic flow and the induced pressure driven flow in the system during the injection stage and then study the fluid velocity in the microchannel caused by the induced space charges in the junction region with an external electric field in the microchannel.

We only discuss the fluid flow in the case when the system is positively biased since the features of the fluid flow in the system are similar when the system is negatively biased. During the injection stage when the system is positively biased, we observed that (i) the electroosmotic flow in the nanochannel generates induced pressure-driven flow in the microchannel, (ii) the fluid flow at the center of the microchannel is dominated by the induced pressure-driven flow, and (iii) fluid circulates in the junction region. When the electrical double layers overlap and the counterion concentration is sufficiently large, the electroosmotic flow in the positively charged nanochannel dominates the electroosmotic flow caused by the negatively charged microchannel such that the fluid flow is from the source channel to the receiving channel. The electroosmotic flow in nanochannel draws the fluid from the source channel into the receiving channel, resulting in a pressure drop across the micro−nano junction regions, as shown in Figure 11. Such induced pressure drops have been used to design electroosmotic pumps using the micro−nano junctions.[2] The direction of electroosmotic flow in the nanochannel and in the microchannels, and the direction of the induced pressure driven flow in the microchannels are shown in Figure 12a. The fluid flow in the microchannel is determined by both the electroosmotic flow and the induced pressure-driven flow. For example, in the receiving channel the pressure pushes the fluid from the junction region to the reservoir, while the direction of the electroosmotic flow is from the reservoir to the junction. The net result is that the fluid flow in the microchannel center region is in the same direction as the pressure-driven flow, but in the opposite direction near the microchannel surface with a velocity profile as shown in Figure 12b. The velocity profile is similar to that typically observed in a combined pressure driven and electroosmotic flow.[33] Figure 13 shows the streamlines of fluid flow near the micro−nano junction regions. The vortices near the entrance of the nanochannel are a result of the opposing directions of the electroosmotic flow and the induced pressure driven flow in the microchannel. The ratio of the pressure gradient to the electrical body force is about one in the junction regions at $t = 15$ ms during the injection. In such a case, there exists a recirculating eddy.[45] Such circulations of the fluid can enhance mixing of analytes in micro−nano devices, which explains the rapid mixing achieved in experiments with micro−nano devices.[13]

Although the electroosmotic flow normally results from the electrical double layer at the surface, Dukhin[46] predicted that the space charges induced by an external electric field could also lead to fluid flow and called it electroosmosis of the second kind. The second kind of electroosmosis has been observed adjacent to ion-permselective particles[47−49] where the space charges

(43) McQuarrie, D. A. *Statistical Mechanics*; University Science Books: Herndon, VA, 2003.
(44) Chan, V. H.; Haddad, S. U. S. Patent 5,856,946, 1999.
(45) Park, S. Y.; Russo, C. J.; Branton, D.; Stone, H. A. *J. Colloid Interface Sci.* **2006**, *297*, 832−839.
(46) Dukhin, S. S. *Adv. Colloid Interface Sci.* **1991**, *35*, 173−196.
(47) Leinweber, F. C.; Tallarek, U. *Langmuir* **2004**, *20*, 11637−11648.

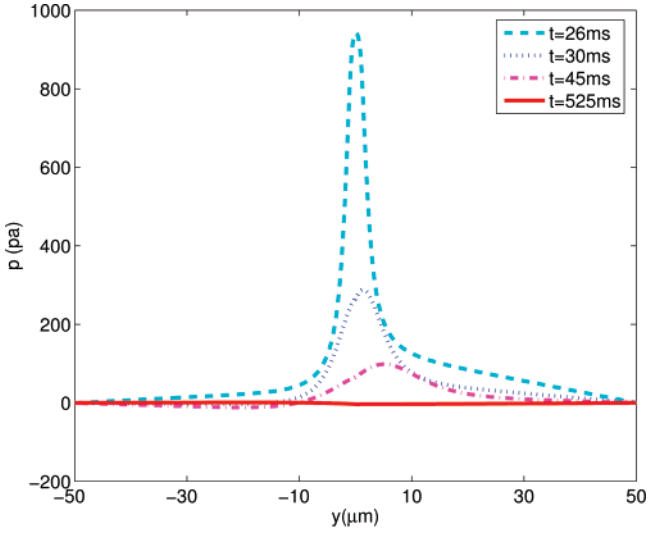

(a)

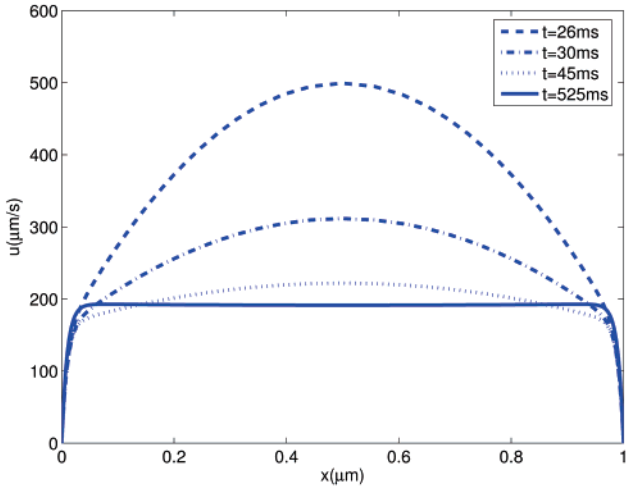

(b)

Figure 17. Pressure and velocity profiles during the recovery stage. (a): Pressure along the central line of the source channel. (b): Velocity profile across the source channel (at $y = 45$ μm).

induced by the applied field on the surface of the particles spread over a larger region than the primary electrical double layer and give rise to highly chaotic flow patterns in the extraparticle void space. High average sample flow speed of the order of 1 mm/s measured in a micro−nano protein preconcentration device, where the expected electroosmotic velocity due to surface charges alone is 10−100 μm/s, has been attributed to electroosmotic flow of the second kind due to induced space charges.[7] In our simulations, we also observed spreading of the space charges over the micro−nano junction region that are capable of inducing electroosmotic flow in the microchannel. During the injection stage when the system is positively biased, the electric field in the nanochannel induces space charges in the source microchannel at the source−nano junction region, as shown in Figure 3a (bottom). After the injection, when the system is switched back to the recovery stage, the net negative space charge undergoes a redistribution and the charge distribution along the center line of the source microchannel at various times during the recovery stage is shown in Figure 14. After injection, the nanochannel is depleted of both cations and anions at the end connected to the source channel, but to satisfy the electroneutrality condition at steady state, it requires more anions than cations. At the start of the recovery, the anions in the source channel from the side of the grounded electrode enter the nanochannel and the anions in the side of the microchannel connected to electrode 1 with the positive potential move toward electrode 1 such that the concentration of the anions on the left side of the source-nano junction region ($t = 26$ ms, -20 μm $< y < 0$ μm) is lower than that of the cations. This causes a net positively charged region on the left side of the junction and a net negatively charged region that remains after the injection on the right side such that there is an electrical double layer formed in the source−nano junction. As recovery progresses, the net charge of the double layer becomes smaller. The 2D contours of the charge density show that the positively charged region and the negatively charged region extend across the whole width of the microchannel at the source−nano junction (Figure 15). The induced space charges in the microchannel cause electroosmotic flow of the second kind in the source microchannel in addition to the electroosmotic flow caused by the microchannel surface charge. Figure 16 shows the streamlines of the flow in the source microchannel caused by the induced charges near the source−nanochannel junction region. At $t = 26$ ms, vortices are generated as the charge redistributes. The space charges induce a large pressure gradient in the junction region (see Figure 17a). Near electrode 2, at $y = 45$ μm, the net flow rate is more than 2.5 times the steady-state electroosmotic flow (see Figure 17b). As recovery progresses, the induced space charge is dispersed and its effect on the net flow diminishes. Although both the depletion zone and the induced space charge contribute to the flow, the major contribution to the flow is from the space charges rather than the depletion region. As shown in Figure 6a, the depletion region is still in the microchannel at $t = 50$ ms, but at $t = 45$ ms the velocity (see Figure 17b) is almost the same as the steady-state velocity. Note that the value of induced space charge is typically proportional to the number of nanochannels and their surface charge densities. For example, using a membrane consisting of 6000 nanochannels extraordinarily large flow rates could be attained in the microchannel.

5. Conclusions

In this paper, we examined the transient operation of a hybrid micro−nano device under rest, injection, and recovery stages using numerical simulations based on coupled PNP and Stokes equations. During the rest stage operation, the coupling between the two microchannels is weak—as a result, independent manipulations can be performed in the microchannels with the nanochannel acting as a gate. During the injection stage, for a positively biased case, depletion and accumulation of ions is observed at the source−nano and receiving−nano junctions, respectively (and vice versa for the negatively biased case). The depletion of the ions in the source−nano junction region gives rise to a net space charge region which gives rise to nonlinear electrokinetic effects during the recovery stage. The variation of the ionic current with time during the recovery stage depends on the nature of injection (positively biased or negatively biased) and rest-stage current is recovered during the steady state. During the injection and recovery stages (prior to steady state), induced pressure, induced electroosmotic flow of the second-kind, and complex circulation of the fluid in the junction regions are observed. Analytical expressions are derived to predict the variation of the ionic current with time during the recovery stage, and they have been shown to capture the basic features of the solution. Finally, using results from analytical expressions, we

(48) Leinweber, F. C.; Tallarek, U. *J. Phys. Chem. B* **2005**, *109*, 21481−21485.
(49) Mishchuk, N. A.; Dukhin, S. S. In *Interfacial Electrokinetics and Electrophoresis*; Delgado, A. V., Ed.; Marcel Dekker, Inc.: New York, 2002.

show that the presence of multiple enrichment−depletion regions in the hybrid micro−nano devices can lead to design and development of a logic device.

Acknowledgment. This work was supported by the NSF under Grants No. 0120978 (the Water CAMPWS Center at UIUC), 0325344, 0328162 (the nano-CEMMS Center at UIUC), 0523435, 0625421, by the NIH under Grant No. PHS 2 PN2 EY016570B, and by the DOE under Grant No. DE FG02 07ER15851.

LA702326V